Photoinduced charge-order melting dynamics in a one-dimensional interacting Holstein model

Hiroshi Hashimoto and Sumio Ishihara
Department of Physics, Tohoku University, Sendai 980-8578, Japan
(Received 28 April 2017; published 31 July 2017)

Transient quantum dynamics in an interacting fermion-phonon system are investigated with a focus on a charge order (CO) melting after a short optical-pulse irradiation and the roles of the quantum phonons in the transient dynamics. A spinless-fermion model in a one-dimensional chain coupled with local phonons is analyzed numerically. The infinite time-evolving block decimation algorithm is adopted as a reliable numerical method for one-dimensional quantum many-body systems. Numerical results for the photoinduced CO melting dynamics without phonons are well interpreted by the soliton picture for the CO domains. This interpretation is confirmed by numerical simulation of an artificial local excitation and the classical soliton model. In the case of large phonon frequencies corresponding to the antiadiabatic condition, CO melting is induced by propagations of the polaronic solitons with the renormalized soliton velocity. On the other hand, in the case of small phonon frequencies corresponding to the adiabatic condition, the first stage of the CO melting dynamics occurs due to the energy transfer from the fermionic to phononic systems, and the second stage is brought about by the soliton motions around the bottom of the soliton band. The analyses provide a standard reference for photoinduced CO melting dynamics in one-dimensional many-body quantum systems.

DOI: 10.1103/PhysRevB.96.035154

I. INTRODUCTION

Ultrafast dynamics in correlated electron systems induced by an intensive optical laser pulse have been widely accepted as an attractive theme in recent solid-state physics [1,2]. The motivation here arises not only from the standpoint of fundamental research in highly nonequilibrium many-body systems but also from the potential applications to efficient energy conversion and ultrafast optical switching. One of the prototypical targets for nonequilibrium many-body systems is the carrier doped and undoped Mott insulators. A variety of exotic nonequilibrium phenomena emerge due to the spin and orbital degrees of freedom [3–11], and a number of theoretical studies have also been performed in the optical induced nonequilibrium state in the Mott insulators [12–21].

Another promising target for photoinduced nonequilibrium dynamics in correlated electron systems is the charge-ordered (CO) state, in which the average electron density per site is 0.5 in most of the cases. The CO states, in which the translational symmetry of the electronic charge distribution is broken, are ubiquitously observed in a wide class of solids. On the verge of the CO, several rich phenomena emerge, such as superconductivity, metal-insulator transition, ferroelectricity, colossal magnetoresistance, and so on. Because the CO system is susceptible to external stimuli due to its small energy scale in comparison with the Mott insulator, this system is a plausible candidate for nonequilibrium electron dynamics research [22–31]. In fact, a variety of CO compounds have been investigated by ultrafast optical pump-probe measurements as well as several time-resolved experimental techniques. In contrast to the Mott insulators, the spin degree of freedom is not expected to play major roles. Instead, the lattice degree of freedom plays crucial roles for equilibrium and nonequilibrium states as follows: (i) The nonuniform electronic charge distribution and the alternate lattice distortion are stabilized cooperatively, (ii) different energy and time scales in the electronic and phononic systems provide a rich variety of transient dynamics, and (iii) energy transfer possibly occurs from the highly excited electronic systems to phononic systems.

Among the several CO systems, the one-dimensional CO insulator is a simple example for study of the nonequilibrium dynamics induced by optical excitation. The organic molecular solid $(TMTTF)_2X$ (X: monovalent anion) is a prototypical one-dimensional CO compound, in which the number of holes per molecular orbital is 0.5 [32–37]. The quantum fluctuation in a low-dimensional lattice promotes strong competition between the long-range CO insulator and the correlated metal and governs the photoinduced transient dynamics between the two states. The quantum nature of lattice vibrations is also crucial for the energy transfer and the relaxation dynamics in nonequilibrium transient states [38–44]. From the theoretical viewpoint, several numerical algorithms have been applied to one-dimensional quantum systems [45–49]. Reliable calculations for one-dimensional systems may provide good references for the highly nonequilibrium transient dynamics in correlated electrons, in which the quantum effect, the many-body effect, and the transient characters are appropriately treated on an equal footing.

In this paper, we address the photoinduced CO melting dynamics in a one-dimensional correlated electron system. In particular, we focus on roles of the quantum fluctuations of electrons and phonons on the transient dynamics. We analyze the one-dimensional spinless fermion model at half filling by using the infinite time-evolving block decimation (iTEBD) method. This method is well accepted as a reliable highly accurate numerical algorithm for the one-dimensional interacting quantum model. In the model without the phonon degree of freedom, CO melting is caused by soliton propagations, corresponding to domain-wall motions in the CO state. In the case of finite fermion-phonon coupling, the transient dynamics depend qualitatively on the adiabatic parameter $\alpha \equiv \omega_0/t$, where ω_0 and t are the phonon frequency and the fermion hopping integral, respectively. In the case of large α, the CO melting occurs in the same way as the case without the phonon degree of freedom and is induced by soliton motions in which the velocity is renormalized by the polaronic effect. On the other hand, in the case of small α, CO melting occurs by the

energy transfer to the phononic system at the first stage and subsequently by the soliton motion around the bottom of the soliton band. The present comprehensive analyses provide a standard reference for the photoinduced CO melting dynamics in one-dimensional systems.

In Sec. II, the fermion-phonon coupled model is introduced, and a numerical method based on the iTEBD algorithm is briefly explained. In Sec. III A, the numerical results for the ground state before photoexcitation are presented. The transient dynamics without the fermion-phonon interaction are introduced in Sec. III B, and the results with the phonon degree of freedom are presented in Sec. III C. Section IV is devoted to a discussion and summary. A detailed formulation for the classical soliton model is given in Appendix.

II. MODEL AND METHOD

The model we use to analyze the photoinduced CO dynamics is the interacting spinless-fermion model on a one-dimensional chain coupled with local phonons. The Hamiltonian is defined as

$$\begin{aligned}\mathcal{H} =& -\sum_i (t_{i,i+1} c_i^\dagger c_{i+1} + \text{H.c.}) \\ &+ V \sum_i \left(n_i - \frac{1}{2}\right)\left(n_{i+1} - \frac{1}{2}\right) \\ &+ \omega_0 \sum_i a_i^\dagger a_i - g \sum_i (a_i + a_i^\dagger)\left(n_i - \frac{1}{2}\right), \end{aligned} \tag{1}$$

where $c_i(c_i^\dagger)$ is the annihilation (creation) operator of a spinless-fermion at site i, $n_i(\equiv c_i^\dagger c_i)$ is the fermion number operator, and $a_i(a_i^\dagger)$ is the annihilation (creation) operator of a local phonon at site i. The first term ($\mathcal{H}_t$) and the second term ($\mathcal{H}_V$) represent the fermion hopping and the Coulomb interaction between fermions in the nearest-neighboring sites, respectively. The third term ($\mathcal{H}_{\text{ph}}$) and the last term ($\mathcal{H}_{\text{ep}}$) represent the phonon energy and the Holstein-type fermion-phonon interaction with a coupling constant g, respectively. As already introduced in Sec. I, $\alpha = \omega_0/t$ is the adiabatic parameter, and $\alpha \ll 1$ and $\alpha \gg 1$ are termed the adiabatic and antiadiabatic limits, respectively. We also introduce the dimension-less fermion-phonon coupling constant $\lambda \equiv g/\omega_0$, which appears in the Lang-Firsov factor shown later.

A light pulse applied along a chain direction is introduced as the Peierls phase in the hopping integral as

$$t_{i,i+1} \rightarrow t e^{iA(\tau)}, \tag{2}$$

where the lattice constant, the light velocity, and the Planck constant are taken to be 1. The vector potential for the pump pulse at time τ is given as

$$A(\tau) = \frac{A_p}{\sqrt{2\pi}\tau_p} e^{-\tau^2/(2\tau_p^2)} \cos(\omega_p \tau), \tag{3}$$

where A_p, ω_p, and τ_p are the amplitude, frequency, and pulse width of the vector potential, respectively. The center of the vector potential is set to $\tau = 0$.

The wave functions for the fermions and phonons in the ground state and the time-evolved states are calculated using the iTEBD method [43,50–53]. The wave function is represented in the matrix-product state form as

$$|\Psi\rangle = \sum_{\sigma_1,\sigma_2,\ldots} \text{Tr}(B^{\sigma_1} B^{\sigma_2} \cdots)|\sigma_1,\sigma_2,\ldots\rangle, \tag{4}$$

where σ_i describes the local states for the fermion and phonon at site i, and B^{σ_i} is a matrix with the dimension χ. The ground-state wave function is obtained by the imaginary-time evolution as

$$|\Psi_{\text{GS}}\rangle \propto \prod_{n=1}^{N} \exp(-\mathcal{H}\delta\tau)|\Psi_0\rangle, \tag{5}$$

where $|\Psi_0\rangle$ is the initial wave function and $\delta\tau$ is the small difference of the imaginary time. Although it is known that this method for searching the ground state is not so efficient in comparison with the variational algorithms [54], this is enough in the present examination. In the calculation for the time-evolved states, $|\Psi(\tau)\rangle$, we use Eq. (5), in which the imaginary time is replaced by the real time as $\delta\tau \rightarrow i\delta\tau$. To calculate the exponential factor in Eq. (5), we adopt the second- and fourth-order Suzuki–Trotter decompositions for the imaginary-time and real-time equations, respectively [55]. It is assumed that the wave functions are invariant under shifts of the two sites in most of the calculations and have a periodicity under shifts of 64 sites in the calculations for the local excitations introduced later. In order to monitor the CO state, we calculate the staggered CO parameter defined as

$$O = \frac{1}{N}\left|\sum_i (-1)^i \left(\langle n_i\rangle - \frac{1}{2}\right)\right|, \tag{6}$$

and the alternate ion displacement defined as

$$q = \frac{1}{N}\left|\sum_i (-1)^i \langle a_i^\dagger + a_i\rangle\right|. \tag{7}$$

Here, $\langle\cdots\rangle$ represents the expectation value with respect to $|\Psi_{\text{GS}}\rangle$ in the ground state and that with respect to $|\Psi(\tau)\rangle$ for the time-evolved state. We define that $\sum_i$ implies a summation up to the number of the inequivalent sites N. For each term of the Hamiltonian in Eq. (1), we introduce the transient energy per site at τ measured from the initial energy defined as

$$\Delta E_X(\tau) = (\langle\Psi(\tau)|\mathcal{H}_X|\Psi(\tau)\rangle - \langle\Psi_{\text{GS}}|\mathcal{H}_X|\Psi_{\text{GS}}\rangle)/N, \tag{8}$$

where X identifies the term of the Hamiltonian.

Accuracies in the numerical calculations are checked by calculating the CO parameter and the ground-state energies for various parameter sets. The present model at $g = 0$, i.e., the interacting spinless fermion model without phonons, is equivalent to the $S = 1/2$ XXZ model in a one-dimensional lattice, and $V = 2t$ corresponds to the Heisenberg model [56,57]. The exact ground state is obtained by the Bethe ansatz [58]: a Luttinger-liquid state as the unique ground state in $V/t < 2$ and the twofold degenerated CO states in $V/t > 2$. Differences in the calculated ground-state energy per site (E_0) from the exact results (E_{exa}), i.e., $|(E_0 - E_{\text{exa}})/E_{\text{exa}}|$, are on the order of 10^{-14} (10^{-9}) at $V/t = 6$ ($V/t = 3$) for $\chi = 64$. The time dependencies of the CO parameter at $g = 0$ and $V/t = 6$ are shown in Fig. 1(a) for various values of χ. It is confirmed that the data for $\chi \geqslant 256$ converge up to $\tau t \simeq 30$.

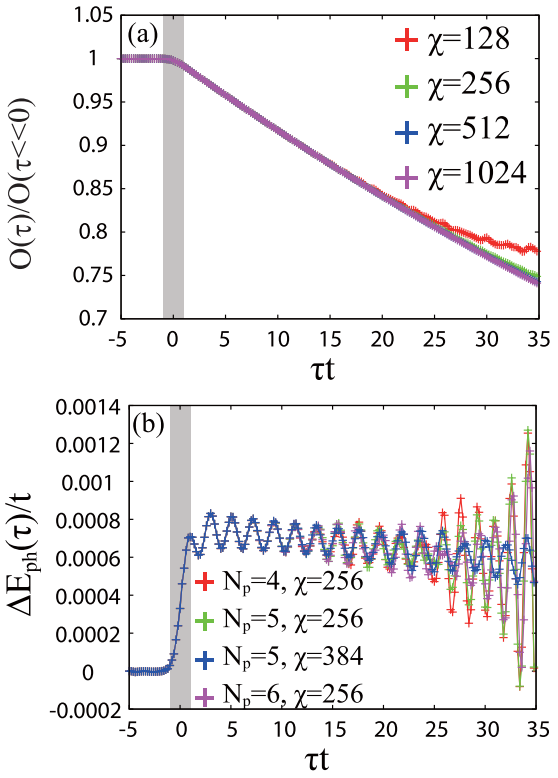

FIG. 1. (a) Time dependencies of the CO parameter for several values of χ at $V/t = 6$ and $g = 0$. Other parameters are chosen as $\omega_p/t = 4$, $A_p = 0.1$, and $\tau_p = 0.01$. (b) Time dependencies of $\Delta E_{\rm ph}$ for several vales of χ and $N_{\rm ph}$. Other parameters are chosen as $\alpha = 3.2$, $\lambda = 1.6$, $\omega_p/t = 6$, $A_p = 0.1$, and $\tau_p = 0.01$. The shaded areas represent the time interval during which the pump pulse is introduced.

In the calculations for $g \neq 0$, the maximum phonon number per site ($N_{\rm ph}$) is truncated. In Fig. 1(b), $\Delta E_{\rm ph}$ are shown for several values of $N_{\rm ph}$ and χ. The calculated results almost converge up to around $\tau t = 25$ at $N_p = 5$ and $\chi = 256$. By taking into account the above results, in most of the numerical calculations for the transient states, we adopt $\chi = 512$ for $g/\omega_0 < 0.5$, $\chi = 384$ for $0.5 \leqslant g/\omega_0 < 1$, and $\chi = 256$ for $1 \leqslant g/\omega_0$ and $N_{\rm ph} = 3{-}8$.

The excitation spectra are calculated on the basis of the matrix-product state formalism, in which finite size clusters of L_c sites with the open boundary condition are adopted. Here the spectral functions are expanded using the Chebyshev polynomial [59]. We define the excitation spectra induced by the operator $\mathcal{A}$ as

$$\chi_{\mathcal{A}A}(\omega) = \langle \Psi_{\rm GS} | \mathcal{A}^\dagger \delta(\omega - \mathcal{H} + E_0) \mathcal{A} | \Psi_{\rm GS} \rangle. \quad (9)$$

The spectral function is expanded as

$$\chi_{AA}(\omega) = \frac{1}{\pi\sqrt{1-\omega^2}} \left[g_0\mu_0 + 2 \sum_{n=1}^{N_{\rm ch}-1} g_n \mu_n T_n(\omega) \right], \quad (10)$$

where $T_n(\omega)$ is the nth Chebyshev polynomial, $\mu_n = \langle \Psi_{\rm GS} | \mathcal{A}^\dagger T_n(\mathcal{H}) \mathcal{A} | \Psi_{\rm GS} \rangle$ is the Chebyshev moment, and g_n is the correction factor defined by

$$g_n = \frac{(N_{\rm ch} - n + 1)\cos\frac{\pi n}{N_{\rm ch}+1} + \sin\frac{\pi n}{N_{\rm ch}+1}\cot\frac{\pi}{N_{\rm ch}+1}}{N_{\rm ch}+1}. \quad (11)$$

From the recursion formula for the Chebyshev vectors, $|t_{n+1}\rangle = 2\mathcal{H}|t_n\rangle - |t_{n-1}\rangle$ with $|t_0\rangle = \mathcal{A}|\Psi_{\rm GS}\rangle$ and $|t_1\rangle = \mathcal{H}|t_0\rangle$, these are calculated in the matrix-product state formalism.

III. RESULTS

A. Ground state

Before discussing the photoinduced dynamics in CO systems, we introduce the ground-state properties as the initial state. In Figs. 2(a) and 2(b), the CO parameter defined in Eq. (6) and the lattice distortions in Eq. (7) for several values of g are presented, respectively. Without the fermion-phonon coupling ($g = 0$), the CO parameter tends to vanish at $V/t = 2$ with decreasing V/t as predicted by the exact solution. With increasing g, the CO phase is strengthened. Alternate ion distortion occurs in the CO phase, and the saturated values of q increase with g.

The optical absorption spectra are shown in Fig. 2(c) for several values of α as well as $g = 0$, and in Fig. 2(d) for several values of λ. We define the optical absorption spectra as

$$\chi_{jj}(\omega) = \langle \Psi_{\rm GS} | j \delta(\omega - \mathcal{H} + E_0) j | \Psi_{\rm GS} \rangle, \quad (12)$$

where $j = \sum_i (itc_i^\dagger c_{i+1} + \text{H.c.})$ is the current operator along the chain. The elementary excitations in the ordered phase of the one-dimensional XXZ model are known as the domain wall motions. The optical absorption spectra, in which the net momentum transfer is zero, are ascribed to the kink and antikink pair with opposite momenta [60,61]. The energy for a pair of the noninteracting kink with momentum k and antikink with momentum k' is given by

$$E(k,k') = \varepsilon_k + \varepsilon_{k'}, \quad (13)$$

with $\varepsilon_k = -2t\cos(2k) + V/2$. This formula indicates that the optical absorption spectra distribute in $V - 4t \leqslant \omega \leqslant V + 4t$, which is consistent with the main part of the optical spectra shown in Fig. 2(c), where $V/t = 6$. We have confirmed that a weak hump structure below $V - 4t$, such as a small peak at around $\omega/t = 1.9$, reduces with increasing cluster size, and this is an artifact due to the size effect. On the other hand, the main structure does not depend sensitively on the cluster size. The spectra in the antiadiabatic case ($\alpha = 3.2$) are similar to the spectra without the fermion-phonon interaction, and some fine structures appear in the adiabatic case ($\alpha = 0.4$). With increasing λ, multiple peak structures appear above the main absorption edge at around $V + n\omega_0$ with an integer number n as shown in Fig. 2(d). In the calculations of the photoinduced dynamics shown in the following section, the pump-photon frequency is chosen around the energy at which $\chi_{jj}(\omega)$ is finite, implying that the pump photon yields resonant excitations.

B. Transient state without the fermion-phonon coupling

In this subsection, the photoinduced CO melting in the case without the fermion-phonon interaction are introduced. In Fig. 3(a), the time profiles of $\Delta E_V(\tau)$ after the excitation are shown for several values of ω_p. We introduce the effective

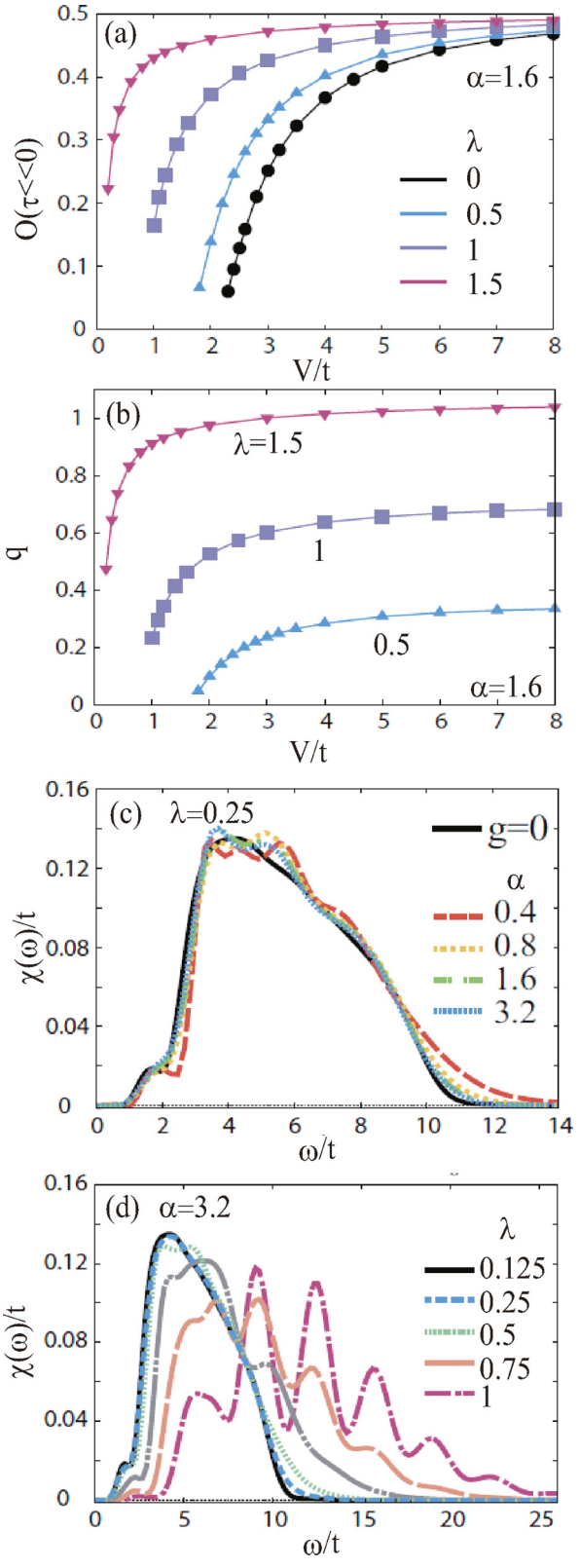

FIG. 2. (a) CO parameter and (b) alternate ion displacement for several values of V/t and λ in the ground state. The other parameter value is chosen as $\alpha = 1.6$. (c) The optical absorption spectra at $\lambda = 0.25$ for several values of α, and (d) the spectra at $\alpha = 3.2$ for several values of λ. The results at $g = 0$ are also shown in (c) for comparison. Other parameters are chosen as $V/t = 6$ and $L_c = 64$ in (c) and (d).

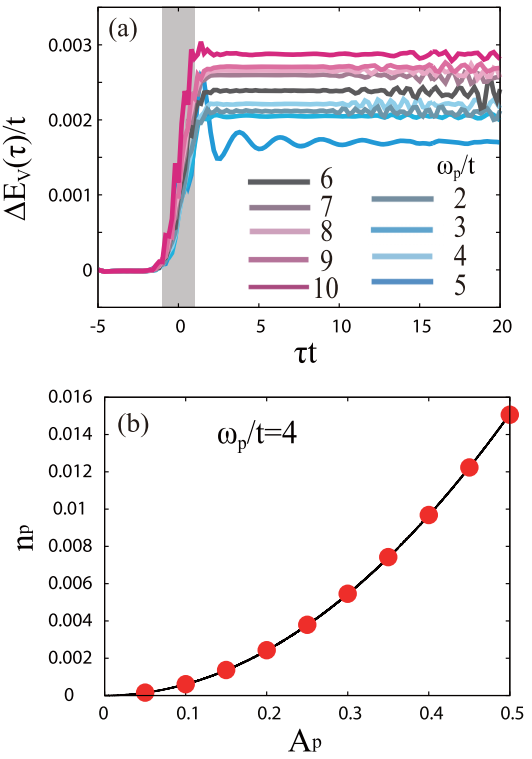

FIG. 3. (a) Time dependence of ΔE_V for several values of ω_p. The shaded areas represent the time interval during which the pump pulse is introduced. (b) The effective absorbed photon number per site at $\omega_p/t = 4$. Other parameter values are chosen as $V/t = 6$ and $g = 0$.

absorbed photon number per site defined as $n_p = N_p(\tau \gg \tau_p)$ with

$$N_p(\tau) = \frac{\Delta E(\tau)}{\omega_p}, \tag{14}$$

where $\Delta E(\tau)$ is the change in the total energy per site. In several cases of ω_p employed in Fig. 3(a), n_p are unified to be approximately 0.0005 by adjusting A_p. After introducing the pump pulse, $\Delta E_V(\tau)$ rapidly increases and settles at almost time-independent values; the photoexcited state is stable after turning off the pump pulse. In the case of small ω_p, an oscillatory behavior appears and is damped at around $\tau = 10/t$. As shown in Fig. 3(b), n_p increases quadratically as a function of A_p. This is interpreted that the number of domain walls in the CO states, i.e., the kinks and antikinks, increases with A_p.

The time profiles of the CO parameter are shown in Fig. 4(a). Reduction in $O(\tau)$ occurs monotonically for all values of A_p. In contrast to the time dependence of $\Delta E_V(\tau)$ shown in Fig. 3(a), the CO melting occurs in a long time scale after turning off the pump pulse. In the case of large A_p, $O(\tau)$ reaches zero, implying almost complete melting of the initial CO. As shown in the semilogarithmic plot in Fig. 4(b), the time dependencies of $O(\tau)$ follow an exponential function as

$$O(\tau) = O_0 \exp(-\gamma\tau), \tag{15}$$

where O_0 is the CO parameter in the initial state, and γ is the damping factor. We have confirmed that exponential dependence of $O(\tau)$ is commonly observed over wide parameter

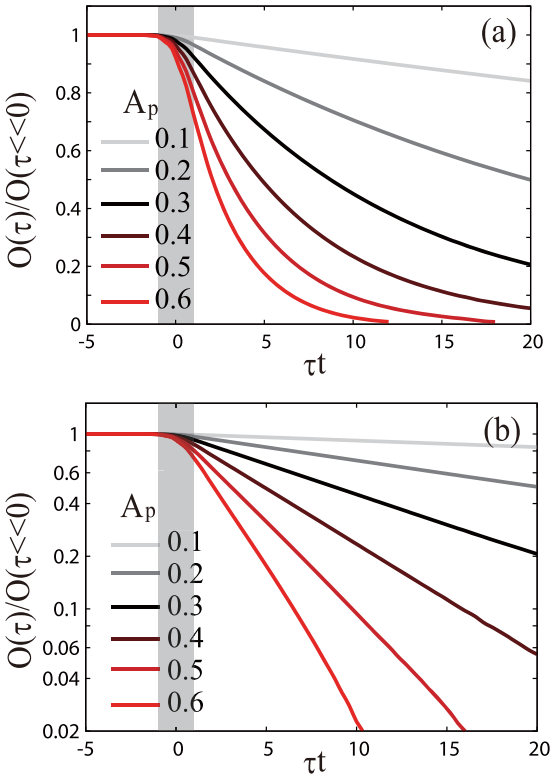

FIG. 4. (a) Time dependencies of the normalized $O(\tau)$ and (b) the semilogarithmic plot of $O(\tau)$ for several values of A_p. The shaded areas represent the time interval during which the pump pulse is introduced. Other parameter values are chosen as $V/t = 6, \omega_p/t = 4$, and $g = 0$.

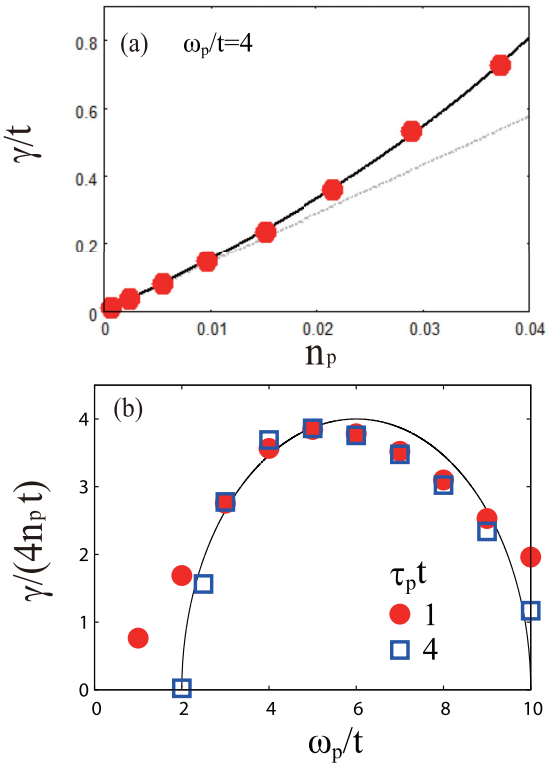

FIG. 5. (a) n_p dependence of γ at $\omega_p/t = 4$. Solid and broken lines represent Eq. (18) and $\gamma = 4vn_p$, respectively. (b) ω_p dependence of $\gamma/(4n_p)$ at $A_p = 0.1$. A solid line represents Eq. (21). The other parameter is chosen as $V/t = 6$.

ranges of ω_p and V. The damping factor is calculated for several values of A_p at fixed $\omega_p(=4t)$ and is plotted as a function of n_p in Fig. 5(a). It increases linearly for small n_p and deviates upward with increasing n_p. As shown in Fig. 5(b), the ω_p dependence of γ shows a dome shape. These two behaviors of γ are well explained by the results of the soliton picture plotted by bold lines in Figs. 5(a) and 5(b), as explained later.

The CO melting dynamics are analyzed by the following artificial electronic excitation. The vector potential for the pump pulse is applied at a specific site instead of the uniform vector potential introduced in Eq. (2). This is termed "the local excitation" from now on and is defined as

$$t_{i,i+1} \to \begin{cases} te^{iA(\tau)} & (i = \cdots -L, 0, L, \cdots) \\ t & \text{other sites,} \end{cases} \tag{16}$$

where L is a periodicity of the sites in which the excitations are induced, and the time dependence of $A(\tau)$ is given in Eq. (3). Responses to the local excitation are monitored by the CO parameter defined at each site termed "the local CO parameter" defined as

$$O_i(\tau) = (-1)^i \left(\langle n_i \rangle - \tfrac{1}{2}\right). \tag{17}$$

An intensity plot of $O_i(\tau)$ induced by the local excitations in a space-time plane is plotted in Fig. 6(a). The periodicity of the local excitations is chosen to be $L = 64$. After introducing the pump pulse, a CO domain characterized by the reduced $O_i(\tau)$ is generated, and the boundaries between the domains propagate almost linearly with time. At $\tau \approx 9/t$, the domain wall collides at $i = \pm 32$ with other domain walls that are generated at $i = \pm L$. After the collision, O_i reduces further. The next collisions occur at approximately $\tau = 18/t$ and $i = 0$. The velocity of the domain wall is approximately four sites per unit time of $1/t$. After the collisions, both the widths and velocities of the domain walls are almost unchanged. From these characteristics, the domain wall dynamics in the photoinduced CO state are identified as the soliton motions. As plotted in Fig. 6(b), the CO parameter $O(\tau)$ calculated from the data of $O_i(\tau)$ shows the exponential decay in the same way as the results in Fig. 4. We conclude that the soliton motions are responsible for the photoinduced CO melting.

Next, we derive the damping factor based on the soliton picture. We set up a model in which the photogenerated solitons are treated as classical particles. A photoinduced fermionic excitation is simulated by a stochastic generation of solitons. We assume that the soliton velocity is constant at v, and the collisions between the solitons are elastic. The details are presented in Appendix. We obtain an expression for γ as

$$\gamma = -\frac{2v \ln(1 - 2Ln_p)}{L}, \tag{18}$$

which is approximately $\gamma = 4vn_p$ in the limit of $n_p \ll 1$. The soliton velocity in Eq. (18) is evaluated from the effective Hamiltonian derived from Eq. (1) in the limit of $V \gg t$. There

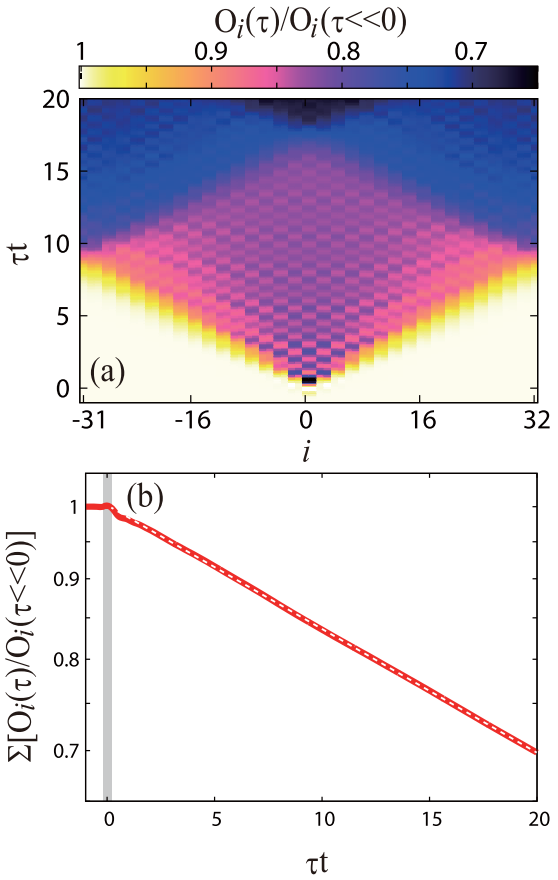

FIG. 6. Numerical results induced by the local excitation. (a) An intensity plot of $O_i(\tau)/O_i(\tau \ll 0)$ in the space-time plane. (b) A semilogarithmic plot of the time profile of $\sum_i[O_i(\tau)/O_i(\tau \ll 0)]$. The shaded areas represent the time interval during which the pump pulse is introduced. The other parameter values are chosen as $V/t = 6$, $g/t = 0$, $\omega_p/t = 6$, $A_p = 0.8$, $\tau_p t = 0.2$, and $L = 64$.

is assumed to be one soliton-antisoliton pair. The effective Hamiltonian is given as [61]

$$\mathcal{H}_{\text{eff}} = -t \sum_{i=\text{odd}} (b_i^\dagger b_{i+2} + d_i^\dagger d_{i+2} + \text{H.c.}) + \frac{V}{2}, \tag{19}$$

where $b_i^\dagger$ (b_i) and $d_i^\dagger$ (d_i) are the creation (annihilation) operators of the hard-core bosons for the soliton and antisoliton, respectively. A summation with respect to i is taken for odd integers. The interaction between the soliton and antisoliton given by the second order of t is not included. The eigenstates are classified by the momenta of the soliton k and antisoliton k', and the eigenenergy coincides with Eq. (13). The group velocity of the soliton is obtained as

$$v_k = |4t \sin 2k|. \tag{20}$$

The factor 2 in the sine function is attributed to the fact that fermion hopping between the nearest neighbor site corresponds to soliton hopping between the next-nearest-neighbor sites. In the case where the photon momenta are zero and the resonant excitation is induced, i.e., $\omega_p = E(k,-k)$, the velocity is represented as a function of ω_p as

$$v_{\omega_p} = \sqrt{(4t)^2 - (\omega_p - V)^2}. \tag{21}$$

The maximum group velocity is given as $4t$, which is consistent with the results in Fig. 6(a).

The analytical expression for the damping factor in Eq. (18) with Eq. (21) is compared with the numerical data. Here, L in Eq. (18) is treated as a fitting parameter and is determined to be approximately $L = 6.5$. It is shown that the n_p dependence of γ plotted in Fig. 5(a) reproduces the calculated data well. As shown in Fig. 5(b), γ as a function of ω_p exhibits a dome-shaped structure that takes its maximum at approximately $\omega_p = V$. This behavior is confirmed by the numerical data for several values of V. The analytical formulation deviates only a little from the numerical data for small V, in which the higher-order quantum fluctuation neglected in Eq. (18) might be important.

C. Effect of the fermion-phonon coupling

In this subsection, the numerical results in the case of $g \neq 0$ are presented. In some numerical calculations, we chose $\alpha = 3.2$ as a typical antiadiabatic limit, in which the iTEBD method provides good efficiency due to the localized characters of phonons. Figure 7(a) shows the time profiles of $O(\tau)$ for several values of α at $\lambda = 0.25$. For comparison, we also present the results at $g = 0$, where $O(\tau)$ decreases exponentially as a function of time as explained previously. With the introduction of the fermion-phonon coupling, the reduction of $O(\tau)$ is suppressed. The exponential decay of $O(\tau)$ remains in the case of large phonon frequencies ($\alpha = 3.2$), but the time profiles of $O(\tau)$ deviate from the exponential decay with decreasing α. To clarify the change in the CO melting dynamics by brought about the fermion-phonon coupling, the concept of the soliton velocity introduced previously is extended to the transient state. From Eqs. (15) and (18) under the conditions $\gamma\tau \ll 1$ and $n_p \ll 1$, we have $O(\tau) \sim e^{-\gamma\tau} \sim 1 - 4vn_p\tau$. Thus, the transient soliton velocity at time τ is introduced as

$$v^*(\tau) = -\frac{1}{4N_p(\tau)} \frac{dO(\tau)}{d\tau}, \tag{22}$$

where $N_p(\tau)$ is defined in Eq. (14). The calculated results of $v^*(\tau)$ are shown in Fig. 7(c). In the case of large α ($\alpha = 3.2$), $v^*(\tau)$ is almost independent of time after turning off the pump pulse in the same way as for $g = 0$. The oscillatory behaviors seen in $\tau \geqslant 10$ are suppressed with increasing χ and are attributed to a numerical artifact. On the other hand, for small α ($\alpha = 0.4$ and 0.8), $v^*(\tau)$ changes remarkably in a short time scale and tends to be saturated in a long time scale. This characteristic time scale in the adiabatic case ($\alpha = 0.4$ and 0.8) will be discussed later. The time profiles of $O(\tau)$ for several values of λ are presented in Figs. 7(b) and 7(d), where α is fixed to be 3.2, i.e., the antiadiabatic condition. The exponential time dependence of $O(\tau)$ and an almost constant $v^*(\tau)$ are observed for $0 \leqslant \lambda \leqslant 3.2$, and $v^*(\tau)$ monotonically decreases with increasing λ. The detailed CO melting dynamics in the cases of the adiabatic and antiadiabatic conditions are explained in the following two subsections.

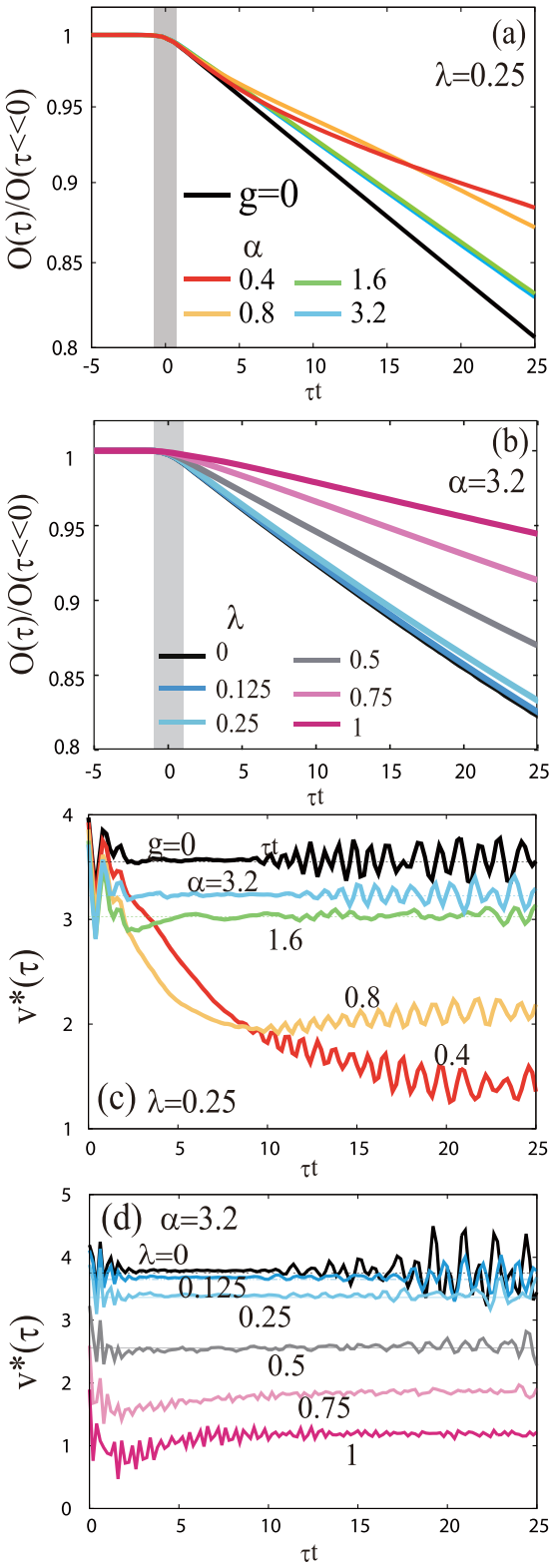

FIG. 7. Time profiles of $O(\tau)$ and $v^*(\tau)$ for [(a) and (c)] several values of α at $\lambda = 0.25$ and $\omega_p/t = 4$ and [(b) and (d)] several values of λ at $\alpha = 3.2$ and $\omega_p/t = 6$. Results at $\lambda = 0$ are also plotted for comparison in (a) and (c). The shaded areas represent the time interval during which the pump pulse is introduced. The oscillatory behaviors which are remarkable in $\tau \geqslant 10$ in (c) and (d) are attributed to a numerical artifact. The other parameter values are chosen as $V/t = 6$, and $\tau_p t = 1$.

1. *Antiadiabatic case ($\alpha \gtrsim 1$)*

First, we focus on the dynamics in the antiadiabatic case at $\alpha = 3.2$ (>1), where the CO parameter decays exponentially. The time profiles of $\Delta E_t(\tau)$ and $\Delta E_{\rm ph}(\tau) + \Delta E_{\rm ep}(\tau)$ are shown for several values of λ in Figs. 8(a) and 8(b), respectively. Except for a small dip and hump structure just after turning off the pump pulse at $\alpha = 2.4$ and 3.2, both of the energies do not show remarkable time dependencies. In the case of $\lambda = 1$ in Fig. 8(b), the energy relaxation occurs at $\tau t \sim 5$ from $\Delta E_{\rm ph}(\tau) + \Delta E_{\rm ep}(\tau)$ to $\Delta E_V(\tau)$ (not shown). With an increase in λ, the saturated value of $\Delta E_t(\tau)$ decreases monotonically. The intensity plots in the space-time plane for $O_i(\tau)$ induced by the local excitation are presented in Fig. 9. For all cases of λ, the soliton motions are stable. As λ increases, the velocity decreases, which is consistent with the results in Fig. 7(d).

From the numerical data shown in Fig. 7(b), the normalized damping rate $\gamma/(4n_p t)$ corresponding to the soliton velocity is plotted as a function of λ in Fig. 10. The velocity decreases monotonically with increasing λ. The bold line in the figure represents the equation given by

$$\gamma/(4n_p t) \propto e^{-g^2/\omega_0^2}, \tag{23}$$

which is expected from the renormalized carrier hopping in the polaronic state based on the Lang-Firsov theory [62]. The analytical formula fits the numerical data well even in the region of small λ, implying that the coherent soliton motion associated with the ion displacement occurs from weak to strong coupling regimes. This is termed the polaronic-soliton picture from now on, and is consistent with the fact that $\Delta E_{\rm ph}(\tau)$ does not show a remarkable change after turning off the pump pulse (not shown). We conclude that, in the antiadiabatic case, the CO melting dynamics is caused by the soliton motion renormalized by the polaron formation.

2. *Adiabatic case ($\alpha \lesssim 1$)*

Next, we focus on the CO melting dynamics in the adiabatic case, $\alpha < 1$, where the time dependence of $O(\tau)$ deviates from the exponential decay as shown in Fig. 7(a). The time profiles of $\Delta E_t(\tau)$ and $\Delta E_{\rm ph}(\tau) + \Delta E_{\rm ep}(\tau)$ are shown for several values of α in Figs. 8(c) and 8(d), respectively. It is confirmed that $\Delta E_V(\tau)$ suddenly increases by pulse irradiation and does not show a remarkable time dependence after turning off the pump pulse (not shown). The time profiles of $\Delta E_t(\tau)$ are clearly different from those in the antiadiabatic case presented in Fig. 8(a); $\Delta E_t(\tau)$ gradually decreases after turning off the pump pulse and is saturated at approximately $\tau t = 10$ and 15 for $\alpha = 0.8$ and 0.4, respectively. Contrary behaviors are observed for $\Delta E_{\rm ph}(\tau) + \Delta E_{\rm ep}(\tau)$, which increases gradually with time. We also confirm that $\Delta E_{\rm ep}(\tau)$ is one order smaller than $\Delta E_{\rm ph}(\tau)$. The interpretation of these results is that the excess energy due to the pump excitation is transferred from the fermionic to phononic systems, and the charge distributions are compatible with the ion displacements.

In order to analyze the energy transfer, the time profiles of $\Delta E_{\rm ph}(\tau) + \Delta E_{\rm ep}(\tau)$ are fitted by a function $C(e^{-\tau/\tau_r} - 1)$, where τ_r is the energy relaxation time and C is a numerical constant. In Fig. 11, the energy relaxation times calculated for several values of $\alpha(<1)$ and λ are plotted as a function

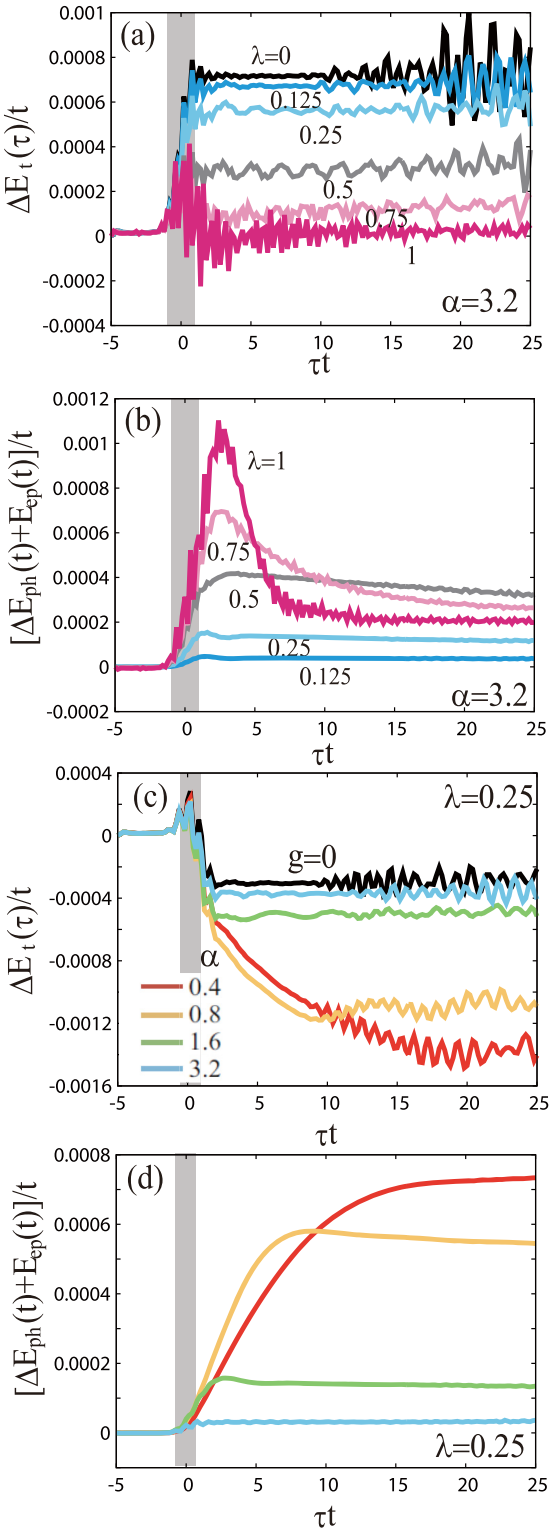

FIG. 8. Time profiles of $\Delta E_t(\tau)$ and $\Delta E_{\rm ph}(\tau) + \Delta E_{\rm ep}(\tau)$ for [(a) and (b)] several values of λ at $\alpha = 3.2$ and $\omega_p/t = 6$ and [(c) and (d)] several values of α at $\lambda = 0.25$ and $\omega_p/t = 4$. Results at $\lambda = 0$ are also plotted for comparison in (a) and (c). The shaded areas represent the time interval at which the pump pulse is introduced. The other parameter values are chosen as $V/t = 6$.

of $g^2/(\omega_0 t)$. An almost linear dependence is observed until $g^2/(\omega_0 t) \sim 0.16$, implying that the energy relaxation is in

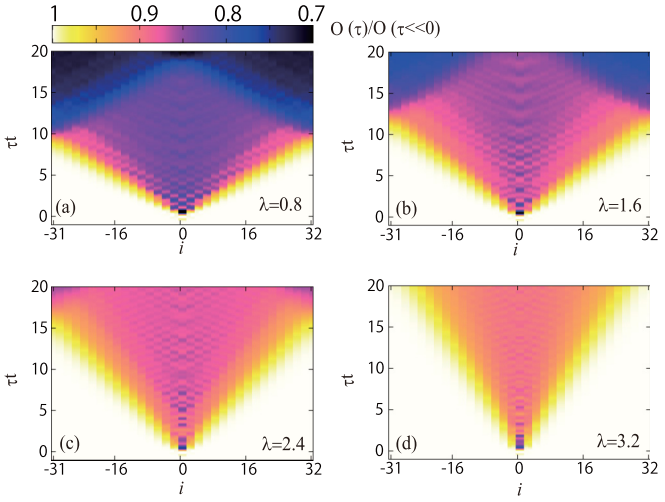

FIG. 9. Intensity plots of $O_i(\tau)$ in the space-time plane for several λ at $\alpha = 3.2$ induced by the local excitations. The other parameter values are chosen as $V/t = 6$, $\omega_p/t = 6$, and $\tau_p t = 0.2$.

accordance with the Fermi golden rule through the fermion-phonon coupling [38–41]. Above $g^2/(\omega_0 t) = 0.16$, the width of the pump pulse chosen to be $\tau_p = 1/t$ is comparable to the energy relaxation time, and the relaxation occurs before turning off the pump pulse. In Figs. 11(b) and 11(c), respectively, intensity maps of $O_i(\tau)$ in the space-time plane after the local excitation are presented for $\alpha = 0.4$ and 0.8 at $\lambda = 0.25$. It is shown that the wave fronts of the domain walls become broad and the averaged velocities decrease with time. This is clearly in contrast to the case of large α (see Fig. 9), in which the soliton velocities are almost independent of time. The reduction of the soliton velocity is explained by the soliton model in Eq. (19): As shown in Eq. (20), the soliton velocity is minimum (maximum) at the bottom (middle) in the soliton band. Thus, the energy relaxation from fermionic to phononic systems leads to the reduction in the velocity, implying a suppression of the CO melting.

Finally, characteristics in the damping factor are summarized; $\gamma/(4n_p t)$ are plotted as a function of the inverse of α in Fig. 12. The damping factors are obtained from

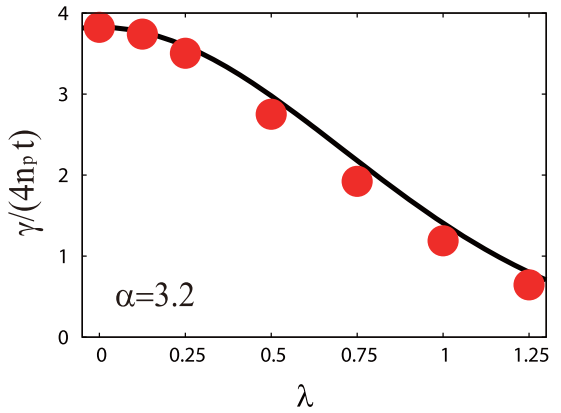

FIG. 10. The normalized damping factor $\gamma/(4n_p)$ as a function of λ at $\alpha = 3.2$. A solid line represents Eq. (23). The other parameter values are chosen as $V/t = 6$, $\omega_p/t = 5$, and $\tau_p t = 1$.

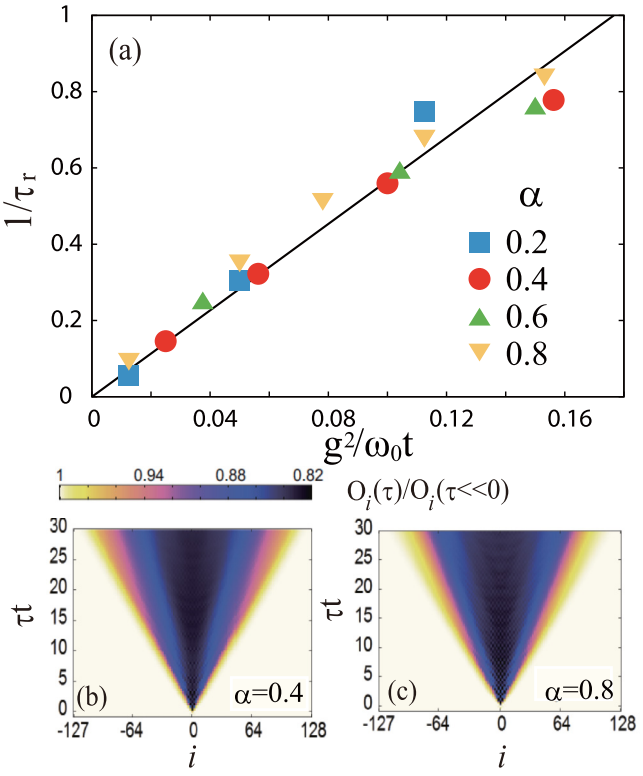

FIG. 11. (a) The inverse of the energy relaxation time as a function of $g^2/(\omega_0 t)$. Data are obtained by fitting $\Delta E_{\rm ph}(\tau) + \Delta E_{\rm ep}(\tau)$ for several values of α using the equation $C(e^{-\tau/\tau_r} - 1)$. Other parameters are chosen as $V/t = 6$, $\omega_p/t = 4$, and $\tau_p t = 1$. The solid straight line is for a guide for the eye. [(b) and (c)] Intensity plots of $O_i(\tau)$ in the space-time plane induced by the local excitation at $\alpha = 0.4$ and 0.8 with $\lambda = 0.25$. The other parameters are chosen as $V/t = 6$, $\omega_p/t = 6$, and $\tau_p t = 0.2$.

the time profiles of $O(\tau)$ at a time when $v^*(\tau)$ is fully saturated. With increasing α, the numerical data approach a red broken line, which represents the damping factor without the fermion-phonon coupling multiplied by the polaronic factor $e^{-(g/\omega)^2}$. Below $\alpha \sim 1$, the reduction of the calculated results from the red broken line is remarkable and is attributable to the energy relaxation from fermionic to phononic systems.

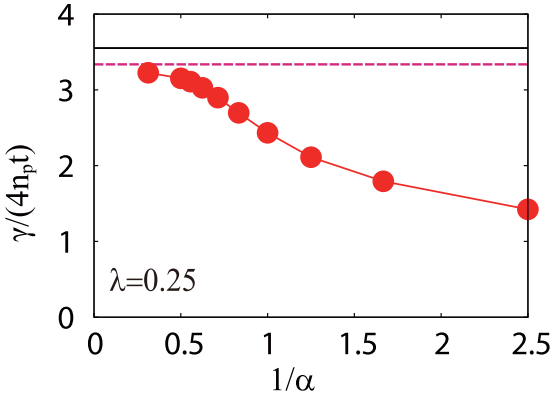

FIG. 12. The normalized damping constant plotted as a function of $1/\alpha$ at $\lambda = 0.25$. Black and red straight lines represent the results at $g = 0$, and $g = 0$ multiplied by $\exp^{-(g/\omega_0)^2}$. The other parameters are chosen as $V/t = 6$, $\omega_p/t = 4$, $A_p = 0.1$, and $\tau_p t = 1$.

IV. DISCUSSION AND SUMMARY

We present in this paper a comprehensive analysis of the photoinduced melting dynamics of the one-dimensional CO state interacting with the local phonons. By using the iTEBD method, we obtain reliable numerical data for the time dependencies of the CO parameter, the electronic and phononic energy, and so on. We also analyze the CO melting dynamics in the system in which the artificial local photoexcitation is introduced. As is well known, the excited state in the one-dimensional CO state without the electron-phonon coupling is described by the soliton and antisoliton picture. This is directly confirmed by calculations of the local CO parameter induced by the local excitation shown in Fig. 6; the domain-wall motions collapse the CO structure and give rise to the exponential time dependence of the CO parameter as $O(\tau) \propto e^{-\gamma\tau}$. The characteristic CO melting induced by the local excitation is reproduced by the classical soliton picture presented in Appendix, in which the solitons are treated as classical particles. We have an expression for the damping constant γ in Eq. (18), showing it is proportional to the soliton velocity in the limit of the weak photoexcitation.

The roles of the quantum phonons in the CO melting dynamics are characterized by the dimensionless adiabatic parameter $\alpha = \omega_0/t$. We perform numerical analyses in a wide parameter region of α. In the case of the antiadiabatic region ($\alpha \gtrsim 1$), the CO melting dynamics are caused by the polaronic soliton picture. The stable propagations of the domain walls survive even when the fermion-phonon coupling is taken into account, but the soliton velocity is renormalized. The damping constant γ decreases with increasing fermion-phonon coupling. This reduction of γ in a wide region of the coupling constant ($0 < \lambda = g/\omega_0 < 1.25$) is well fitted by the expression for the polaronic state deduced by Lang and Firsov, [62] which is known to be derived in the strong-coupling regime. This implies that the solitons and ionic displacements propagate coherently even in the case of small g. This might be attributed to the fact that the ions are distorted cooperatively in the CO ground state even for small g, where incoherent motions of electrons and ions produce an energy loss on the macroscopic order.

On the contrary, in the adiabatic case ($\alpha \lesssim 1$), the CO melting in the early stage of the photoexcited transient state is not induced by the propagations of the solitions but by their relaxations. The photogenerated solitons have a band energy of $\varepsilon_k = -2t \cos 2k$ and a velocity $v = 4t \sin 2k$, where the interaction with phonons and that between solitons are neglected. Through the fermion-phonon coupling, the kinetic energy of the solitons is dissipated to the phononic system, and the soliton velocity is reduced. The solitons settle down around the bottom of the band, where they cannot be relaxed further by the emission of the quantum phonons. After the relaxation, CO melting is induced by the soliton propagation in the same way as in the antiadiabatic case. This scenario is confirmed by the calculation of the transient electron energy and phonon energy, in which the relaxation time is scaled by $g^2/(\omega_0 t)$. The change in the time dependence of the CO parameter,

that is, the nonexponential decay in the early stage and the exponential decay after the energy relaxation, is understood in this scenario.

Beyond the present calculations in the one-dimensional lattice, the photoinduce CO melting in the two- and three-dimensional CO systems is expected to be caused by the individual electronic motions instead of the soliton motions. It is shown in the two-dimensional lattice that the time profiles of the CO parameter after photoirradiation do not follow simple exponential dependencies, and there are threshold fluorescences which increase with increasing the electron-phonon coupling [30,31]. Further reliable analyses are required to clarify the common and different points between the photoinduced CO dynamics in one- and higher-dimensional systems.

ACKNOWLEDGMENTS

We thank M. Naka, H. Seo, and S. Iwai for their helpful discussions. This work was supported by MEXT KAKENHI Grants No. 26287070, No. 15H02100, and No. 17H02916. Some of the numerical calculations were performed using the facilities of the Supercomputer Center, the Institute for Solid State Physics, the University of Tokyo.

APPENDIX: A CLASSICAL SOLITON MODEL

In this Appendix, we introduce a classical model for the photoinduced soliton and antisoliton in order to derive an analytical expression for the damping factor given in Eq. (18). We introduce a classical particle model in a one-dimensional chain, in which hard-core particles (antiparticles) correspond to the solitons (antisolitons) in the CO state. We assume that the (anti)particle velocity is constant at v, and elastic collisions occur between the (anti)particles. Pump-photon irradiation is simulated by a stochastic generation of the particle-antiparticle pairs in the bonds connecting the nearest-neighboring sites with a periodicity L and probability n. We assume a π phase shift for CO and a step-function-like CO parameter across the (anti)soliton as shown in Fig. 13(a). The local CO parameter is calculated in this model and the intensity map of $O_i(\tau)$ in the space-time map is shown in Fig. 13(b). The result reproduces the numerical results shown in Fig. 6(a) well. At time $\tau_m = Lm/(2v)$ when the m-time collision occurs as indicated by broken lines in Fig. 13(b), the local order parameters are spatially uniform. We confirm at least up to $m = 5$ that the amplitude of the CO parameter at time τ_m is given approximately by $O(\tau_m) = (1-2n)^m$. This result is

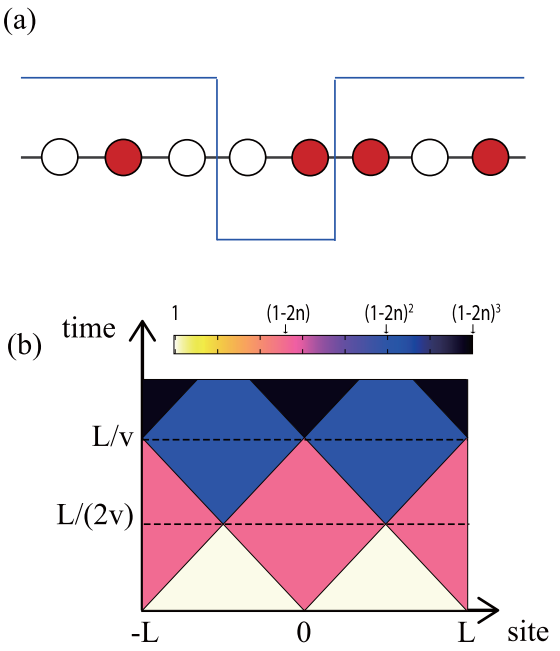

FIG. 13. (a) A schematic picture of a soliton and an antisoliton in the CO state. (b) An intensity map of $O_i(\tau)$ in the space-time plane obtained by the classical soliton model.

interpreted as follows. Let us consider the state at $\tau_1 = L/(2v)$, until when the (anti)solitons propagate independently. The local CO parameters at the sites that the (anti)soliton passes over and does not pass over are 1 and -1, respectively. Because the probability of the photogeneration of solitons is n, the CO parameter at this time is obtained by averaging as $O(\tau_1) = 1 \times (1-n) + (-1) \times n = 1 - 2n$. At time $\tau_2 = 2L/(2v)$, the second collision occurs between the soliton and antisoliton generated at $i = 0$ and L. Four photoinduced states are possible: The (anti)soliton is generated at both the sites of $i = 0$ and L, at either the $i = 0$ site or the $i = L$ site, and at neither of the sites. Because these probabilities are n^2, $n(1-n)$, $n(1-n)$, and $(1-n)^2$, respectively, the CO parameter is obtained by their average as $O(\tau_2) = 1 \times n^2 + (-1) \times n(1-n) + (-1) \times n(1-n) + 1 \times (1-n)^2 = (1-2n)^2$. The order parameters at τ_m with $m \geqslant 3$ are obtained in the same way. By using the relation $n = n_p L$ where n_p is the effective photon number introduced in Sec. III B, the CO parameter is given as $O(\tau_m) = (1-2n)^m = \exp[2v\tau_m \ln(1-2Ln_p)/L]$. This expression can be extended to continuous time. By comparing this result with Eq. (15), the damping factor for the CO parameter is identified as $\gamma = -2vL^{-1}\ln(1-2Ln_p)$, which is Eq. (18).

[1] *Photo-Induced Phase Transitions*, edited by K. Nasu (World Scientific, New Jersey, 2004).
[2] Y. Tokura, J. Phys. Soc. Jpn. **75**, 011001 (2006).
[3] S. G. Han, Z. V. Vardeny, K. S. Wong, O. G. Symko, and G. Koren, Phys. Rev. Lett. **65**, 2708 (1990).
[4] K. Matsuda, I. Hirabayashi, K. Kawamoto, T. Nabatame, T. Tokizaki, and A. Nakamura, Phys. Rev. B **50**, 4097 (1994).
[5] S. Iwai, M. Ono, A. Maeda, H. Matsuzaki, H. Kishida, H. Okamoto, and Y. Tokura, Phys. Rev. Lett. **91**, 057401 (2003).
[6] H. Okamoto, T. Miyagoe, K. Kobayashi, H. Uemura, H. Nishioka, H. Matsuzaki, A. Sawa, and Y. Tokura, Phys. Rev. B **83**, 125102 (2011).
[7] F. Novelli, G. D. Filippis, V. Cataudella, M. Esposito, I. Vergara, F. Cilento, E. Sindici, A. Amaricci, C. Giannetti, D. Prabhakaran,

S. Wall, A. Perucchi, S. D. Conte, G. Cerullo, M. Capone, A. Mishchenko, M. Gruninger, N. Nagaosa, F. Parmigiani, and D. Fausti, Nat. Commun. **5**, 5112 (2014).
[8] L. Stojchevska, I. Vaskivskyi, T. Mertelj, P. Kusar, D. Svetin, S. Brazovskii, and D. Mihailovic, Science **344**, 177 (2014).
[9] A. Cavalleri, C. Tóth, C. W. Siders, J. A. Squier, F. Raksi, P. Forget, and J. C. Kieffer, Phys. Rev. Lett. **87**, 237401 (2001).
[10] C. Kübler, H. Ehrke, R. Huber, R. Lopez, A. Halabica, R. F. Haglund, Jr., and A. Leitenstorfer, Phys. Rev. Lett. **99**, 116401 (2007).
[11] L. Perfetti, P. A. Loukakos, M. Lisowski, U. Bovensiepen, M. Wolf, H. Berger, S. Biermann, and A. Georges, New J. Phys. **10**, 053019 (2008).
[12] A. Takahashi, H. Itoh, and M. Aihara, Phys. Rev. B **77**, 205105 (2008).
[13] T. Oka and H. Aoki, Phys. Rev. Lett. **95**, 137601 (2005).
[14] J. K. Freericks, V. M. Turkowski, and V. Zlatic, Phys. Rev. Lett. **97**, 266408 (2006).
[15] B. Moritz, T. P. Devereaux, and J. K. Freericks, Phys. Rev. B **81**, 165112 (2010).
[16] F. Heidrich-Meisner, I. Gonzalez, K. A. Al-Hassanieh, A. E. Feiguin, M. J. Rozenberg, and E. Dagotto, Phys. Rev. B **82**, 205110 (2010).
[17] P. Werner, T. Oka, M. Eckstein, and A. J. Millis, Phys. Rev. B **81**, 035108 (2010).
[18] L. Vidmar, J. Bonča, T. Tohyama, and S. Maekawa, Phys. Rev. Lett. **107**, 246404 (2011).
[19] M. Mierzejewski, L. Vidmar, J. Bonča, and P. Prelovšek, Phys. Rev. Lett. **106**, 196401 (2011).
[20] H. Lu, S. Sota, H. Matsueda, J. Bonča, and T. Tohyama, Phys. Rev. Lett. **109**, 197401 (2012).
[21] E. Iyoda and S. Ishihara, Phys. Rev. B **89**, 125126 (2014).
[22] V. Kiryukhin, D. Casa, J. P. Hill, B. Keimer, A. Vigliante, Y. Tomioka, and Y. Tokura, Nature **386**, 813 (1997).
[23] D. Polli, M. Rini, S. Wall, R. W. Schoenlein, Y. Tomioka, Y. Tokura, G. Cerullo, and A. Cavalleri, Nat. Mater. **6**, 643 (2007).
[24] P. Beaud, A. Caviezel, S. O. Mariager, L. Rettig, G. Ingold, C. Dornes, S.-W. Huang, J. A. Johnson, M. Radovic, T. Huber, T. Kubacka, A. Ferrer, H. T. Lemke, M. Chollet, D. Zhu, J. M. Glownia, M. Sikorski, A. Robert, H. Wadati, M. Nakamura, M. Kawasaki, Y. Tokura, S. L. Johnson, and U. Staub, Nat. Mater. **13**, 923 (2014).
[25] S. Iwai, K. Yamamoto, A. Kashiwazaki, F. Hiramatsu, H. Nakaya, Y. Kawakami, K. Yakushi, H. Okamoto, H. Mori, and Y. Nishio, Phys. Rev. Lett. **98**, 097402 (2007).
[26] H. Ichikawa, S. Nozawa, T. Sato, A. Tomita, K. Ichiyanagi, M. Chollet, L. Guerin, N. Dean, A. Cavalleri, S. Adachi, T. Arima, H. Sawa, Y. Ogimoto, M. Nakamura, R. Tamaki, K. Miyano, and S. Koshihara, Nat. Mater. **10**, 101 (2011).
[27] K. Onda, S. Ogihara, K. Yonemitsu, N. Maeshima, T. Ishikawa, Y. Okimoto, X. Shao, Y. Nakano, H. Yamochi, G. Saito, and S. Y. Koshihara, Phys. Rev. Lett. **101**, 067403 (2008).
[28] K. Iwano, Phys. Rev. Lett. **102**, 106405 (2009).
[29] J. Rincon, K. A. Al-Hassanieh, A. E. Feiguin, and E. Dagotto, Phys. Rev. B **90**, 155112 (2014).
[30] H. Hashimoto, H. Matsueda, H. Seo, and S. Ishihara, J. Phys. Soc. Jpn. **83**, 123703 (2014).
[31] H. Hashimoto, H. Matsueda, H. Seo, and S. Ishihara, J. Phys. Soc. Jpn. **84**, 113702 (2015).
[32] T. Ishiguro, K. Yamaji, and G. Saito, *Organic Superconductors* (Springer, New York, 1998).
[33] C. S. Jacobsen, D. B. Tanner, and K. Bechgaard, Phys. Rev. B **28**, 7019 (1983).
[34] L. Balicas, K. Behnia, W. Kang, E. Canadell, P. Auban-Senzier, D. Jerome, M. Ribault, and J. M. Fabre, J. Phys. I (France) **4**, 1539 (1994).
[35] M. Dressel, M. Dumm, T. Knoblanch, and M. Masino, Crystals **2**, 528 (2012).
[36] P. Monceau, F. Y. Nad, and S. Brazovskii, Phys. Rev. Lett. **86**, 4080 (2001).
[37] Y. Naitoh, Y. Kawakami, T. Ishikawa, Y. Sagae, H. Itoh, K. Yamamoto, T. Sasaki, M. Dressel, S. Ishihara, Y. Tanaka, K. Yonemitsu, and S. Iwai, Phys. Rev. B **93**, 165126 (2016).
[38] P. Werner and M. Eckstein, Europhys. Lett. **109**, 37002 (2015).
[39] S. Sayyad and M. Eckstein, Phys. Rev. B **91**, 104301 (2015).
[40] Y. Murakami, P. Werner, N. Tsuji, and H. Aoki, Phys. Rev. B **91**, 045128 (2015).
[41] D. Golež, J. Bonča, L. Vidmar, and S. A. Trugman, Phys. Rev. Lett. **109**, 236402 (2012); **111**, 119901(E) (2013).
[42] J. D. Lee, Phys. Rev. B **80**, 165101 (2009).
[43] F. Dorfner, L. Vidmar, C. Brockt, E. Jeckelmann, and F. Heidrich-Meisner, Phys. Rev. B **91**, 104302 (2015).
[44] G. De Filippis, V. Cataudella, E. A. Nowadnick, T. P. Devereaux, A. S. Mishchenko, and N. Nagaosa, Phys. Rev. Lett. **109**, 176402 (2012).
[45] N. Maeshima and K. Yonemitsu, J. Phys. Soc. Jpn. **74**, 2671 (2005).
[46] N. Maeshima and K. Yonemitsu, Phys. Rev. B **74**, 155105 (2006).
[47] N. Maeshima and K. Yonemitsu, J. Phys. Soc. Jpn. **76**, 074713 (2007).
[48] K. Iwano, Phys. Rev. B **84**, 235139 (2011).
[49] K. A. Al-Hassanieh, J. Rincon, E. Dagotto, and G. Alvarez, Phys. Rev. B **88**, 045107 (2013).
[50] G. Vidal, Phys. Rev. Lett. **98**, 070201 (2007).
[51] S. Takayoshi, M. Sato, and T. Oka, Phys. Rev. B **90**, 214413 (2014).
[52] A. Ono, H. Hashimoto, and S. Ishihara, Phys. Rev. B **94**, 115152 (2016).
[53] A. Ono, H. Hashimoto, and S. Ishihara, Phys. Rev. B **95**, 085123 (2017).
[54] U. Schollwöck, Ann. Phys. **326**, 96 (2011).
[55] N. Hatano and M. Suzuki, Lect. Notes Phys. **679**, 37 (2005).
[56] F. Mila and X. Zotos, Europhys. Lett. **24**, 133 (1993).
[57] S. Ejima, F. Gebhard, and S. Nishimoto, Europhys. Lett. **70**, 492 (2005).
[58] L. Samaj and Z. Bajnok, *Introduction to the Statistical Physics of Integrable Many-Body Systems* (Cambridge University Press, Cambridge, UK, 2013).
[59] A. Holzner, A. Weichselbaum, I. P. McCulloch, U. Schollwöck, and J. von Delft, Phys. Rev. B **83**, 195115 (2011).
[60] N. Ishimura and H. Shiba, Prog. Theor. Phys. **63**, 743 (1980).
[61] Y. Kanamori, H. Matsueda, and S. Ishihara, Phys. Rev. B **82**, 115101 (2010).
[62] I. G. Lang and Y. A. Firsov, Sov. Phys. JETP **27**, 443 (1968).